JOURNAL PRE-PROOF

This is an early version of the article, published prior to copyediting, typesetting, and editorial correction. The manuscript has been accepted for publication and is now available online to ensure early dissemination, author visibility, and citation tracking prior to the formal issue publication.

It has not undergone final language verification, formatting, or technical editing by the journal's editorial team. Content is subject to change in the final Version of Record.

To differentiate this version, it is marked as "PRE-PROOF PUBLICATION" and should be cited with the provided DOI. A visible watermark on each page indicates its preliminary status.

The final version will appear in a regular issue of *Archives of Acoustics*, with final metadata, layout, and pagination.

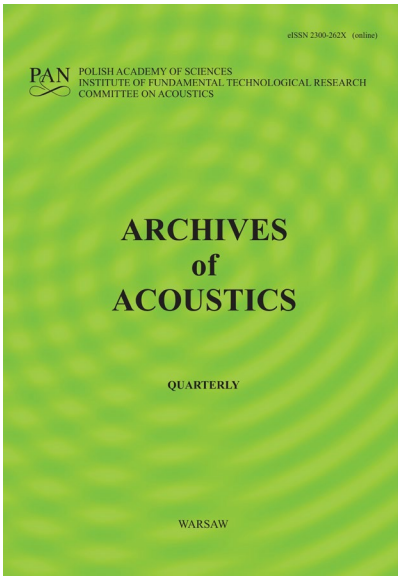

Title: Broadband Vibration-Isolating Metamaterial for MRI-Induced Vibrations

Author(s): Swapnil Arawade, Janusz Piechowicz

DOI: https://doi.org/10.24423/archacoust.2026.4359

Journal: *Archives of Acoustics*

ISSN: 0137-5075, e-ISSN: 2300-262X

Publication status: In press

Received: 2025-10-22

Revised: 2026-01-30

Accepted: 2026-26-04

Published pre-proof: 2026-05-04

Please cite this article as:

Arawade S., Piechowicz J. (2026), Broadband Vibration-Isolating Metamaterial for MRI-Induced Vibrations, *Archives of Acoustics*, https://doi.org/10.24423/archacoust.2026.4359

Broadband Vibration-Isolating Metamaterial for MRI-Induced Vibrations

Swapnil ARAWADE[1*], Janusz PIECHOWICZ[2]

[1] https://orcid.org/0000-0003-1571-050X

[2] https://orcid.org/0000-0002-1435-4673

Department of Mechanics and Vibroacoustics, AGH University of Krakow, Kraków, Poland

*Corresponding Author e-mail: sarawade@agh.edu.pl

Abstract

The magnetic resonance imaging (MRI) is an important diagnostic tool in medical field. The vibrations originated from the gradient coil of MRI system leads to loud operational noise. The study explores the numerical investigation of elastic metamaterial for attenuation of MRI induced vibrations that could radiate as sound at air-structure interface. The elastic metamaterials with embedded resonators can significantly attenuate the wave propagation by opening a local resonance bandgap. In this study the wave propagation properties of two models of elastic metamaterial are analysed. The dispersion diagrams are studied with parametric analysis investigating the influence of the different geometric features on the bandgap generation. The model the metamaterial was analysed with finite element analysis to investigate the wave attenuation performance. The frequency analysis of the multicellular model showed high transmission loss corresponding to the bandgaps in calculated dispersion diagrams. The results revealed that, the optimum model of the metamaterial showed overlap of 72.3 % with the vibration frequency range of the MRI scanner and the frequency analysis of the multicellular arrangement reported transmission loss up to 115.7 dB. These results demonstrate the potential of the such elastic metamaterial for targeted vibro-acoustic control and provide a framework for design of structures for wave attenuation in sensitive acoustic environments.

Keywords: Elastic metamaterials, local-resonance bandgap, vibro-acoustic coupling, MRI noise, wave attenuation.

Acronyms

2D – two-dimensional,

a – lattice constant of unit cell in metamaterial,

BGC – Bandgap coverage.

d_1 – diameter of the hard inclusion,

FEA – finite element analysis,

IBZ – irreducible Brillouin zone,

MRI – magnetic resonance imaging,

TL – transmission loss,

w – thickness of soft wrapping layer.

1. Introduction

The Magnetic resonance imaging (MRI) is a very important tool in medical diagnosis without use of harmful ionizing radiations (Bruno *et al*., 2019; Reda *et al*., 2021; Landini *et al*., 2018). For generating images MRI system utilises static magnetic field, dynamic magnetic field gradient and radio frequency pulses. The interaction of static magnetic field and gradient field leads to generation of Lorentz force setting the gradient coil in vibration. This vibration propagates to surface and its vibro-acoustic coupling with surrounding air generates the typical MRI noise (Zhang *et al*., 2025; Leo, D'Orazio, 2025; Hedeen, Edelstein, 1997; Mansfield *et al*., 1998; Moelker, *et al*., 2003). Literature have reported the sound pressure level reaching up to 133 dB, which may induce anxiety, fear, and potential temporary loss of hearing (Moelker, Pattynama, 2003; Hutter *et al*., 2018; Arawade, Piechowicz, 2024a; 2024b). Also, this vibration also propagates through structure and reaches to scanning zone reducing the quality of image with blurring and or unknown artifacts (Gallichan *et al*., 2010; Fuhrer *et al*., 2019; Frollo *et al*., 2007). Generally, MRI noise and vibration are present in frequency range of 300 Hz to 3000 Hz with major peaks observed between 1000 Hz to 2000 Hz. Many approaches have been explored to reduce generation and propagation of the MRI vibration and noise such as modifying input electric current pulses to gradient coil, gradient coil modification, active and passive noise control (McJury, 2022; Kanal *et al*., 1992; AlMeer, 2022; Li *et al*., 2011; Lee *et al*., 2017; Lasota, Meller, 2020). In addition to the system level approaches, significant industrial efforts have been directed towards vibration isolation and structural decoupling of MRI equipment from its surrounding. AMC MECANOCAUCHO offers their Vibrabsorber + Sylomer® mounts, which effectively minimizes the vibration propagation (AMC MECANOCAUCHO, 2025). Kinetic noise control offers precision isolation systems including elastomeric isolators, to mitigate airborne and structure-borne noise (Kinetic noise control, 2025). Unisorb presents an engineered isolation materials, such as IB-500^{TM} blocks for minimizing vibrations (Unisorb Installation Technologies, 2025). International Design

Engineering (IDE) delivers both passive and active vibration isolators to enhance MRI imaging performance (International Design Engineering, 2025). Additionally, acoustic panels and floating ceiling and wall treatments are also commonly employed in the MRI rooms to absorb airborne noise and enhance the room acoustics (Acoustical Surface Inc, 2008; Faraday Shielding and Design Pvt Ltd, 2025). Despite these developments, most existing solutions focus on isolating the MRI scanner or treating the room and do not directly suppress vibroacoustic couplings at panel. This highlights the need for strategies that address vibration attenuation at the source.

Metamaterials (Kumar *et al*., 2022; Wei *et al*., 2025; Wu *et al*., 2025; Zhang, Zhao, 2025) are the artificial materials which shows special tailored properties that the natural materials do not have. Metamaterials are explored for different counterintuitive properties such as frequency bandgaps (Miao *et al*., 2025; Liu *et al*., 2025), cloaking (Ahmad *et al*., 2025; Fu *et al*., 2025), negative refraction (Ruks *et al*., 2025; Zhou *et al*., 2025), negative mass density (Hao *et al*., 2025; Wang *et al*., 2025) and negative Poisson's ratio (Li, 2025; Shunshun, Zhao, 2025). Mechanical metamaterials are type of metamaterials having properties designed to regulate the propagation of elastic waves. Literature shows that their properties are highly influenced by structural parameters instead of only composition of constituent materials (Chua *et al*., 2025; He *et al*., 2024). The elastic metamaterials are composed of periodic composites of two or more materials with dissimilar mechanical properties leading to the generation of elastic bandgaps in wave dispersion. The elastic waves cannot propagate in the frequency range of bandgap and hence this property of elastic metamaterials make them important for potential application in vibration isolation and damping.

The methods to obtain the bandgap over specific frequency range are mainly classified as Bragg scattering effect and local resonance mechanism (Kaina *et al*., 2013). Phononic crystals based metamaterials having scatterers embedded in host material utilizes principle of Bragg scattering for wave propagation control. In this method wave reflection and interference among the periodic structure leads to formation of frequency dependant bandgap restricting wave propagation at specific frequencies (Chuang *et al*., 2020; Liu, Zhu, 2019). Phononic crystals show bandgap when the structural periodicity is on the order of the wavelength, where bandgap characteristics typically depend upon lattice arrangement, scatterer size, contrast of impedance between the constituent materials in unit cell (Qi *et al*., 2018; Xiang *et al*., 2020). These cellular structures show high strength to mass ratio favourable in different applications requiring robust and broad bandgaps (Wen *et al*., 2020; Wickeler, Naguib, 2020). The phononic crystals are

majorly suitable for high frequency applications because of the requirement of destructive interference of waves between the periodic cells. In case of low to mid frequency range vibration control using the Bragg scattering phononic crystals becomes impractical due to requirement of larger size of structure (Zhao *et al*., 2024). The local resonance metamaterial based on periodic structure was first introduced by Liu *et al*., in early 2000s, achieving subwavelength bandgaps using local resonance in structure (Liu *et al*., 2000). The locally resonant metamaterials work on the principle of negative indexes where the frequency dependant properties become negative in the tuned frequency range . In this negative property region, the local resonators oscillate with maximum potential which provides restoration forces opposing the incoming excitation and elastic/ acoustic waves cannot propagate through the structure (Lee, Wright, 2016; Lee *et al*., 2022). The resonating units are have been reported as spring mass systems, Helmholtz resonators, mass on membrane resonators, etc [Hu *et al*., 2016; Li *et al*., 2022; Peiró-Torres *et al*., 2019; Naify *et al*., 2010). Modification of design parameters such as mass, stiffness, damping and geometry, local resonance metamaterials can be tuned to attenuate the specific targeted frequencies (Fan *et al*., 2021; Hu *et al*., 2021). local resonance metamaterials show smaller lattice cells with low to mid frequency bandgaps highlighting potential in multiple applications of structural monitoring, vibration, and noise mitigation (Ma, Sheng, 2016; Pires *et al*., 2022). Generally, they show narrow bandgaps and research is actively going on to optimize locally resonant metamaterial to produce wide bandgaps.

Despite extensive research in the field of metamaterials, very few studies have explored their potential to control the vibration and noise from MRI systems. This work explores the inverse design of locally resonant elastic metamaterial specifically targeting the vibration frequencies generated from the gradient coil of the MRI scanner that propagate and couple to acoustic field at air structure interface. The local resonance mechanism is selected because it enables the formation of band gaps within the target low to mid frequency range using subwavelength unit cells, resulting in a compact design suitable for the confined geometry of the MRI system. Dispersion relation analysis is employed to characterize intrinsic wave propagation behaviour of periodic cell and identify the subwavelength resonance induced bandgaps that govern the attenuation behaviour. The study investigates the influence of constituent materials and geometric parameters on bandgap generation and vibration attenuation performance by using finite element method. By designing the bandgap corresponding to the MRI system vibration spectra, this investigation presents a systematic methodology for designing the metamaterial for targeted vibro-acoustic control in sensitive medical environments.

2. Model and Methods

This section mainly presents the structure of the locally resonant elastic metamaterial and introduces the method for evaluation of dispersion characteristic curve and transmission loss spectrum of the elastic metamaterial using the solid mechanics module of the numerical simulation software COMSOL, followed by material compatibility analysis.

2.1. Design of the elastic metamaterial

The study focuses on the 2D elastic metamaterial having periodic arrangement in XoY plane and uniform structure in Z direction. The inclusion material is considered to be isotropic hard solid periodically embedded in the soft matrix material. The unit cell has square lattice structure with the lattice constant a representing the distance between the two adjacent unit cells. The diameter of the inclusion is denoted by d_1. The study includes analysis of two models, first model consists a hard solid in single soft matrix, while second model consists hard inclusion wrapped by an additional layer of soft elastic material and embedded together in soft matrix. The thickness of soft material wrapping is denoted by w. The construction of the proposed models and corresponding unit cells are shown in Fig. 1.

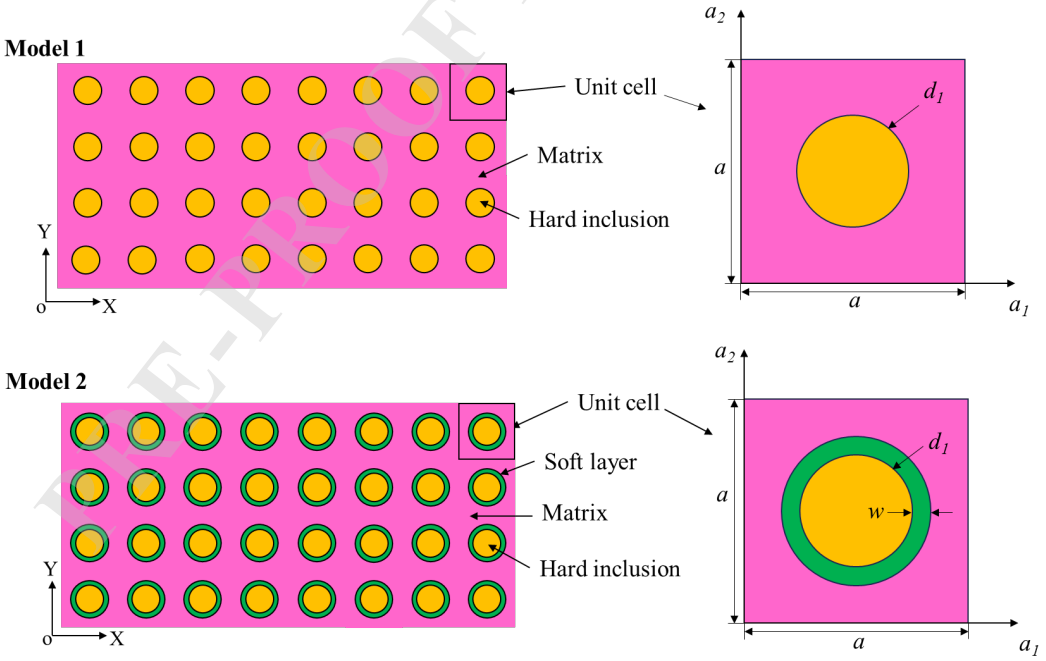

Fig. 1. Structural schematic of the elastic metamaterial presenting configuration of metamaterials models and their unit cell geometries.

The metamaterial layer is The initial geometric parameters of the unit cell are presented in Table

1. In this study, in addition to non-magnetic nature, chemical inertness and corrosion resistance are critical attributes that are required by constituent materials to ensure the suitability for application in MRI environment. Therefore, the proposed metamaterial has tungsten as solid inclusion, silicone (polysiloxane) polymer as host elastic matrix and soft rubber as a wrapping layer. The mechanical material properties considered for numerical model are presented in the Table 2.

Table 1. Geometric parameters in the model.

Parameter	Symbol	Value	Unit
Lattice constant of unit cell	a	5	[mm]
Diameter of hard inclusion	d_1	3	[mm]
Thickness of the soft wrapping layer	w	0.2	[mm]

Table 2. Material properties in the model.

Material	Density [kg/m^3]	Modulus of elasticity [GPa]	Poisson's ratio
Tungsten	18950	360	0.28
Silicone	1080	4.5E-03	0.46
Rubber	1300	1.175E-04	0.47

In the MRI system, the gradient coil system is usually cylindrical with the radius approximately $R \approx 300$ mm. In this study the maximum size of metamaterial unit cell is constrained below $a = 8$ mm. This yields the curvature parameter $a/R = 0.026$. This small ratio indicates a weakly curved configuration, for which the structure can be locally approximated as planar at the scale of the unit cell. Consequently, the plane wave hypothesis employed in the dispersion analysis remains valid for the considered frequency range. In addition, the silicone host has low elastic modulus which allows it to conform to the cylindrical geometry of the MRI bore with negligible curvature induced stress at the unit cell scale. Considering these conditions, the mechanical excitation of the metamaterial layer base can be approximated as locally uniform and curvature effects are not expected to significantly influence the local resonant bandgap characteristics.

2.2. Finite element analysis

To characterize the intrinsic wave propagation behaviour of the periodical metamaterial presented in model 1 and 2, dispersion relation analysis is performed using eigenfrequency formulation. This approach enables identification of subwavelength bandgaps associated with the locally resonant unit cell in which wave propagation is restricted. By solving the Bloch-Floquet eigenvalue problem for single unit cell, the dispersion relations are obtained

independently for finite size and boundary effects, providing the fundamental basis for prediction of vibration attenuation. The theoretical background and conceived method for calculation of dispersion diagram is explained in this section (Sun et al., 2022; Huang et al., 2021; Li et al., 2023; Yang et al., 2023; Tang et al., 2024). The direct basic vectors in orthogonal cartesian coordinates are $a_1 = a(1,0)$ and $a_2 = a(0,1)$. In the reciprocal space these vectors are represented as follows:

$$b_1 = \frac{2\pi}{a}(1,0);\ b_2 = \frac{2\pi}{a}(0,1)\ . \tag{1}$$

Finite element analysis method enables evaluation of dispersion diagram by solving the extreme values of multi order eigenfrequencies in the first Brillouin zone. The square lattice of unit cells has $1/8^{th}$ symmetry and the corresponding irreducible Brillouin zone (IBZ) with key points of highest symmetry Γ, X and M are shown in the Fig. 2

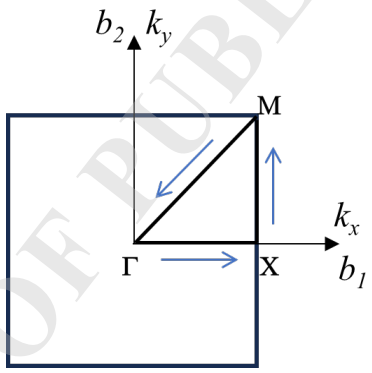

Fig. 2. Illustration of irreducible Brillouin zone Γ-X-M in the square lattice unit cell

The wave propagation in the linear elastic, periodic lattice media is expressed with following governing equation:

$$-\rho\omega^2\boldsymbol{u} = (\lambda+\mu)\nabla(\nabla\cdot\boldsymbol{u}) + \mu\nabla^2\boldsymbol{u}\ . \tag{2}$$

where u is the displacement vector and ω is the angular frequency, ρ is density, ∇ is Hamilton operator, λ and μ are the Lamé constants of the constituent materials,

According to the Bloch-Floquet theory, an infinite structure with a lattice constant can be substituted by a unit cell for basic calculation. Bloch-Floquet theorem gives displacement field of periodic media as:

$$\boldsymbol{u}(\boldsymbol{r},\boldsymbol{t}) = \boldsymbol{u}(\boldsymbol{r})e^{i\omega \boldsymbol{t}} . \quad (3)$$

where $\boldsymbol{t}$ is time, $\boldsymbol{r} = (x, y)$ is position vector and ω is the angular frequency.

The displacement vector $\boldsymbol{u}(\boldsymbol{r})$ can be expressed as,

$$\boldsymbol{u}(\boldsymbol{r}) = U(\boldsymbol{r})e^{-i\boldsymbol{k}\cdot\boldsymbol{r}} . \quad (4)$$

where $U(r)$ is the eigenvalue amplitude, $\boldsymbol{k}$ =(k_x,k_y) is Bloch wave vector. The displacement $\boldsymbol{u}(\boldsymbol{r})$ is also periodic consistent to function of lattice vector $\boldsymbol{R}$ (Bravais lattice vector), which is expressed as:

$$\boldsymbol{u}(\boldsymbol{r} + \boldsymbol{R}) = U(\boldsymbol{r}) . \quad (5)$$

Thus, the displacement u satisfies the following relation,

$$\boldsymbol{u}(\boldsymbol{r} + \boldsymbol{R}) = e^{i\boldsymbol{k}\cdot\boldsymbol{r}}\boldsymbol{u}(\boldsymbol{r}) . \quad (6)$$

This relation is applied as a boundary condition to the outer edges of the unit cell in the x and y direction. Combining the governing equation with these boundary conditions yields a standard eigenvalue problem,

$$(\boldsymbol{K} - \omega^2\boldsymbol{M})\boldsymbol{q} = \boldsymbol{F} . \quad (7)$$

Where, $\boldsymbol{K}$ is stiffness matrix, $\boldsymbol{M}$ is mass matrix, $\boldsymbol{q}$ and $\boldsymbol{F}$ are generalised displacement and force vectors, respectively. The formulated eigenvalue problem is solved numerically by using eigenfrequency analysis in COMSOL Multiphysics. The dispersion relation is calculated by sweeping Bloch wave vector k along the edges of IBZ. The finite element model of the metamaterial cell for evaluation of dispersion relations was discretised by using free triangular mesh. The mesh density was defined based on the smallest geometrical feature of the model. Particularly, for model 2 with thin wrapping layer of soft rubber around tungsten, minimum of 2 finite elements were ensured across the thickness of the layer. Mesh refinement study was performed to ensure numerical accuracy, confirming results are insensitive to further increase in mesh density.

To maintain the applicability of the elastic metamaterial in the MRI system to attenuate the vibration produced by the gradient coil, the size of the metamaterial was limited within 40 mm in Y direction. The parametric analysis was performed to investigate the influence of the

geometric features in the model 1 and model 2. The lattice constant a was varied from 5 mm to 8 mm, diameter d_1 of hard inclusion was varied from 3 mm to 7.5 mm and thickness w of rubber layer was varied from 0.1 mm to 0.7 mm. Further, the bandgap coverage (BGC) percentage was calculated to investigate the suitability of the metamaterial to attenuate MRI vibrations, the expression is as follows:

$$\%\, BGC = \left(\frac{\sum_{j=1}^{M} \max\left(0, \left(\min\left(f_{d2}, {f_{g2}}^{(j)}\right) - \max\left(f_{d1}, {f_{g1}}^{(j)}\right)\right)\right)}{f_{d2} - f_{d1}} \right) \times 100 \qquad (8)$$

where, f_{d1} and f_{d2} are lower and upper limit of desired bandgap, M is total number of bandgaps in the desired frequency range and ${f_{g1}}^{(j)}$ and ${f_{g2}}^{(j)}$ are lower and upper limit of j^{th} obtained bandgap, respectively.

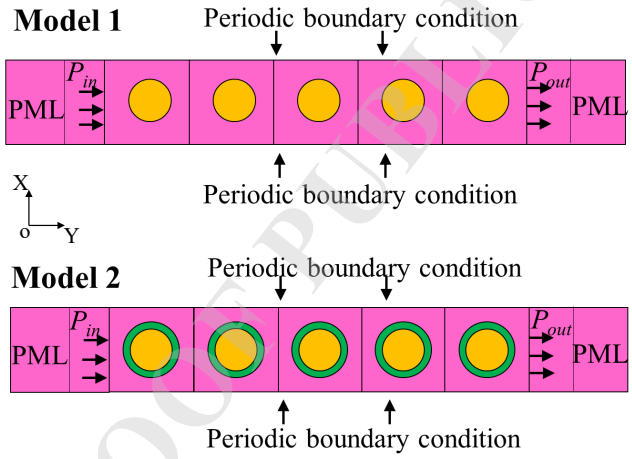

Fig. 3. Finite element analysis setup for evaluation of transmission loss in Y direction through multicellular arrangement of metamaterial cells

The frequency-domain analysis was performed to evaluate transmission loss (TL) of the finite number of cells of elastic metamaterial, validating the band structure obtained from the eigenfrequency analysis. In the 2-Dimensional XoY model, the transmission loss are evaluated along the radial (Y) direction, corresponding to the direction normal to the MRI panel surface. The FEA model to calculate the transmission loss is shown in Fig. 3. Both the models were meshed with free triangular elements with mesh setup and refinement checks consistent with those performed in the dispersion analysis. The harmonic excitation displacement with frequency ranging from 0 – 3000 Hz was given as input to the first cell of elastic metamaterial and output was measured at the end of last cell. The TL is calculated as,

$$TL = 20\ \log_{10}\left(\frac{P_{in}}{P_{out}}\right) \tag{9}$$

where P_{out} is output displacement and P_{in} is input displacement. The artificial domain known as perfectly matched layer (PML) was considered on input and output side of the model. The transmission loss was calculated for number of iterations varying the geometrical parameter of model 1 and model 2 elastic metamaterial.

2.3 MRI compatibility analysis of selected material

While sections 2.1 and 2.2 presented mechanical necessity of the selected materials to achieve specific wave propagation characteristics, it is also crucial to verify their electromagnetic compatibility for integration into an MRI scanner. This sections analyses the electromagnetic characteristics of the constituent materials to ensure they do not disturb the imaging process. The properties such as magnetic susceptibility and electrical conductivity are particularly important to decide whether the structure may perturb the static magnetic field, influence the gradient field distribution or induce currents during MRI operation. In the presented metamaterial models, the primary components are tungsten rods as inertial resonators, silicone as the host and a soft rubber as additional layer around the tungsten rods specifically in second model.

2.3.1 Influence of magnetic susceptibility on field homogeneity

Tungsten is a paramagnetic material with volume magnetic susceptibility approximately $\chi_v \approx 76 \times 10^{-6}$, calculated from the reported mass susceptibility of $\chi_{mass} = 4 \times 10^{-9}$, m^3/kg (Enghag, 2008) with industrial grade density of 18950 kg/m^3. The silicone has volume diamagnetic susceptibility of $\chi_v = -8.03 \times 10^{-6}$ for RTV 615 silicone, which is comparable to the water and biological tissue (Wapler et al., 2014). Soft rubber is diamagnetic material and show volume susceptibility in the order of $\chi_v \approx -1 \times 10^{-5}$ (Callister et al., 2013). As a result, the overall contrast introduced by the elastomeric components is minimal.

As discussed by Schenck, the localized susceptibility mismatch induced magnetic field distortion (ΔB) decays with distance (s) according to the inverse-cubic relation, $\Delta B \propto 1/s^3$, where s is the scalar distance from the susceptibility inclusion (Schenck, 1996). Given the relatively weak susceptibility contrast of tungsten compared to ferromagnetic materials and peripheral placement of the metamaterial relative to the scanning volume, any field distortion decays substantially before reaching the isocentre, resulting to negligible influence on the global field homogeneity and linearity of the gradient within the scanning volume. For context, the

volume magnetic susceptibility of tungsten is approximately half than that of titanium alloys commonly used in MRI conditional implants (Kajima et al., 2020; Chiba et al., 2019).

2.3.2 Influence of electrical conductivity and eddy currents

In the MRI system, the dynamic magnetic fields from gradient coils are known to induce eddy currents responsible for heating, electromotive force and torque on the conductor and imaging artifacts. Tungsten is an electrically conductive material and could, principally support the induced eddy currents when exposed to time-varying gradient magnetic fields. The magnitude of eddy current and heating effect in typical MRI environment strongly depends on geometry, location and orientation of the conductor [Buchli et al., 1998; Stroud et al., 2019; Lee et al., 2024].

The tungsten rods are oriented parallel to the main magnetic field, which minimizes magnetically induced displacement and torque. While time-varying transverse gradient magnetic fields are perpendicular to the rod axis and may induce the eddy currents within the conductor. However these currents are expected to remain localize and limited in the magnitude due to design features of the metamaterial. Each tungsten rod is encapsulated by dielectric silicone in model 1 while model 2 has an additional layer of dielectric rubber is wrapped around the tungsten rods. This configuration prevents electrical continuity between the adjacent tungsten inclusions, consequently minimizing the possibility of large scale conduction loop and resulting eddy current heating. Additionally, relatively small diameter of tungsten rod minimizes the effective loop area exposed to changing magnetic flux, further reducing the eddy current amplitudes.

Considering the radio frequency (RF) pulses during MRI scan, RF field couples with the conductor in the MRI scan bore and induces heat at the tips of the conductor. The heating effect is maximum when the length of conductor is corresponding to the half of the RF excitation wavelength in MRI scanning, known as antenna effect (Mattei et al., 2008; Winter et al., 2019). Taking advantage of 2D design of the metamaterial, the length of the tungsten rod can be explicitly controlled to make them electrically short compare to the RF wavelength at clinical field strength by minimizing their ability to resonate with RF field. Furthermore, the rods are embedded in dielectric material ensuring galvanic isolation from the scanner and subject. The isolation limits the RF induced eddy current pathways and to limit conduction loops.

Based on the above considerations, the selected materials support the assumption that the proposed structure introduce negligible perturbation to the MRI magnetic field, and minimum eddy current generation, with effective vibration control through local resonance mechanism.

3. Results and Discussion

This section presents the band structure of the elastic metamaterial model 1 and model 2 using the method mentioned in previous section. The mechanism of bandgap formation and parametric influence on characteristic are thoroughly investigated. Furthermore, transmission loss is evaluated through the frequency-domain analysis as an indicator of reduced vibro-acoustic coupling.

3.1. Bandgap characteristics and vibration modes

In the beginning, first 8 eigenfrequencies were considered for calculation of dispersion curves. The dispersion relations obtained from the eigen frequency analysis of the model 1 in its initial configuration (a = 5 mm; d_1 = 3 mm) are shown in Fig. 4. The dispersion relations of model 1 notably show a complete bandgap highlighted in grey region, where the upper limit of the eigenfrequency solutions was observed to be above 11000 Hz. As per requirement of the application in MRI scanner the bandgap should appear for the frequency range of 300 Hz to 3000 Hz. To assess the validation of the dispersion curve characteristics with the initial configuration of model 1, the transmission loss characteristics were observed in the frequency range 0 – 12000 Hz as depicted in Fig. 4.

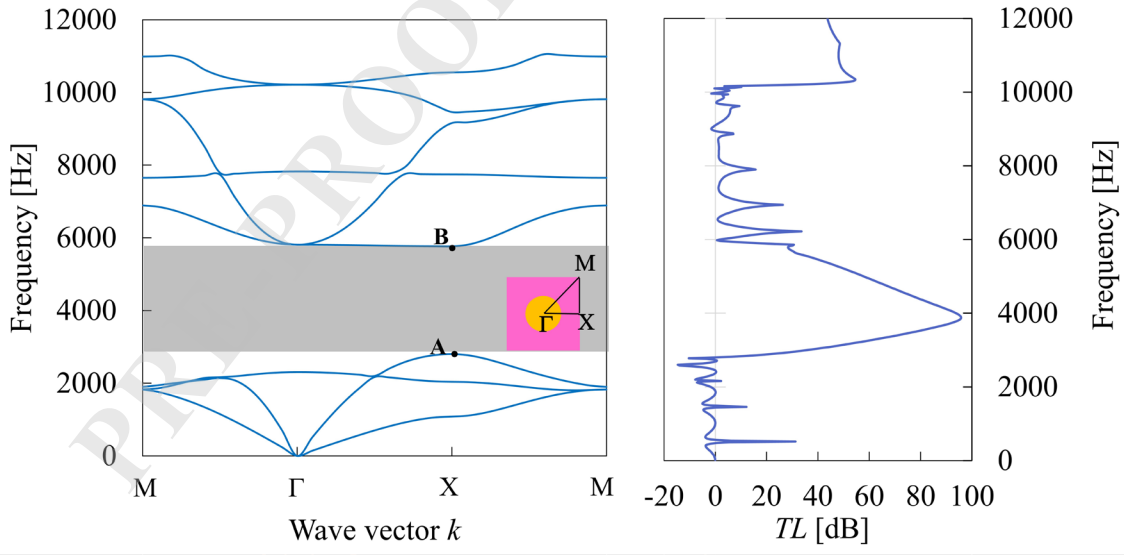

Fig. 4. The dispersion diagram of elastic metamaterial model 1 presenting the identified bandgap shaded in grey region with A and B points representing lower and upper limits of bandgap accompanied by transmission loss spectrum

It is evident that the dispersion curves of the model 1 exhibits a single ultrawide complete

bandgap starting from 2804.4 Hz to 5765.7 Hz between 3rd and 4th eigenfrequency relation. The attenuation peak exceeding the 76 dB within the bandgaps, with an average transmission loss exceeding 58 dB within the forbidden band. The vibration attenuation region in transmission loss spectrum roughly corresponds to the attenuation region of the bandgap observed in dispersion curve, providing strong validation for the accuracy of the calculated dispersion diagram. The overall BGC concerning the MRI vibration range of model 1 was obtained to be 7.24% for the given configuration. The vibration modes corresponding to point A and B indicating the upper and lower limit of the bandgap in model 1 are shown in Fig. 5. The colour of the model surface indicates the amplitude of the vibration, showing red colour as maximum displacement and blue corresponding to minimum displacement.

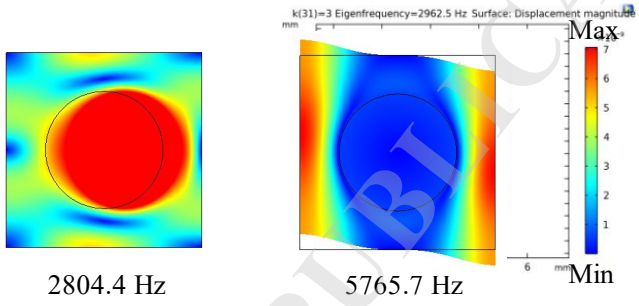

Fig. 5. Vibration modes of bandgap in model 1 at point A and B shown in dispersion diagram

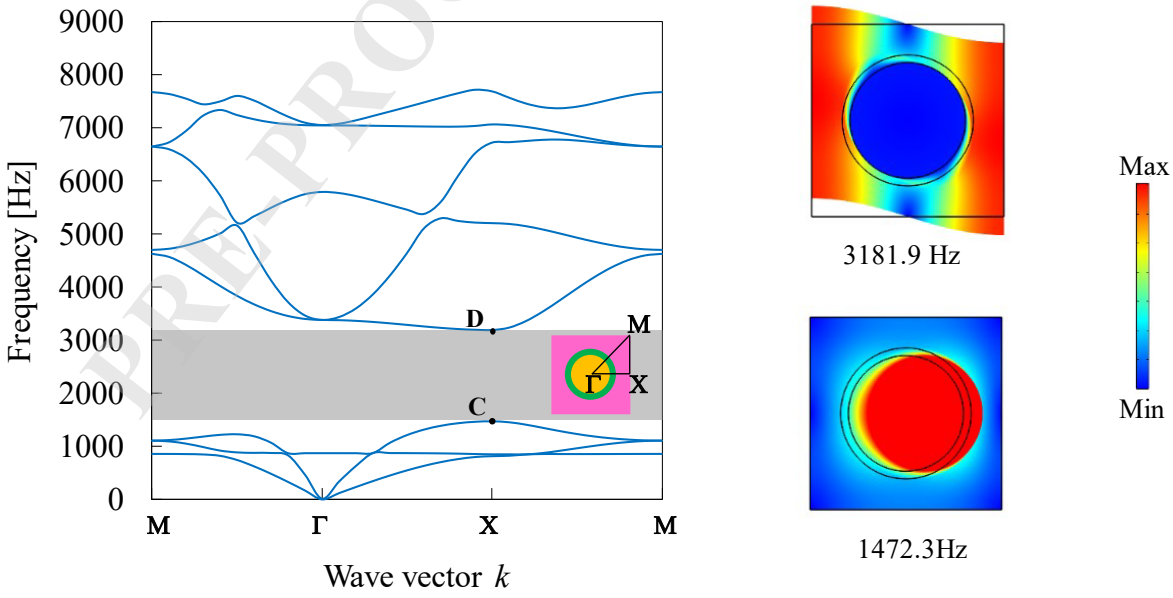

Fig. 6. Dispersion diagram of elastic metamaterial model 2 depicting bandgap in grey region with bandgap vibration modes at points C and D

The model 2 of elastic metamaterial was analysed with the similar configuration of unit cell of model 1(a = 5 mm; d_1 = 3 mm) and thickness of soft wrapping layer w = 0.2 mm. To maintain the consistency in the method. the analysis was limited to first 8 eigen frequencies and the dispersion relation was calculated and plotted as shown in Fig. 6. The model 2 also shows single wide complete bandgap starting from 1472.3 Hz and closing on 3181.9 Hz. The presence of soft layer around the hard inclusion shifted the bandgap in lower frequencies. The vibration mode shapes corresponding to the opening and closing of bandgap at points C and D are presented in Fig. 6. The BGC calculated for the analysed configuration of model was obtained to be 56.57 %.

3.2. Parametric analysis of metamaterial models

After obtaining the bandgap closer to the desired frequency range, the influence of the geometric parameters for both the models of elastic metamaterials was explored. The diameter d_1 of the hard inclusion was varied from 3 mm to 0.5 mm less than the lattice constant a with increment step of 0.5 mm. During the further analysis, the lattice constant parameter a was varied from 5 mm to 8 mm, with incremental step of 1.0 mm. The variation in the obtained bandgap characteristics of model 1 are shown in the Fig. 7.

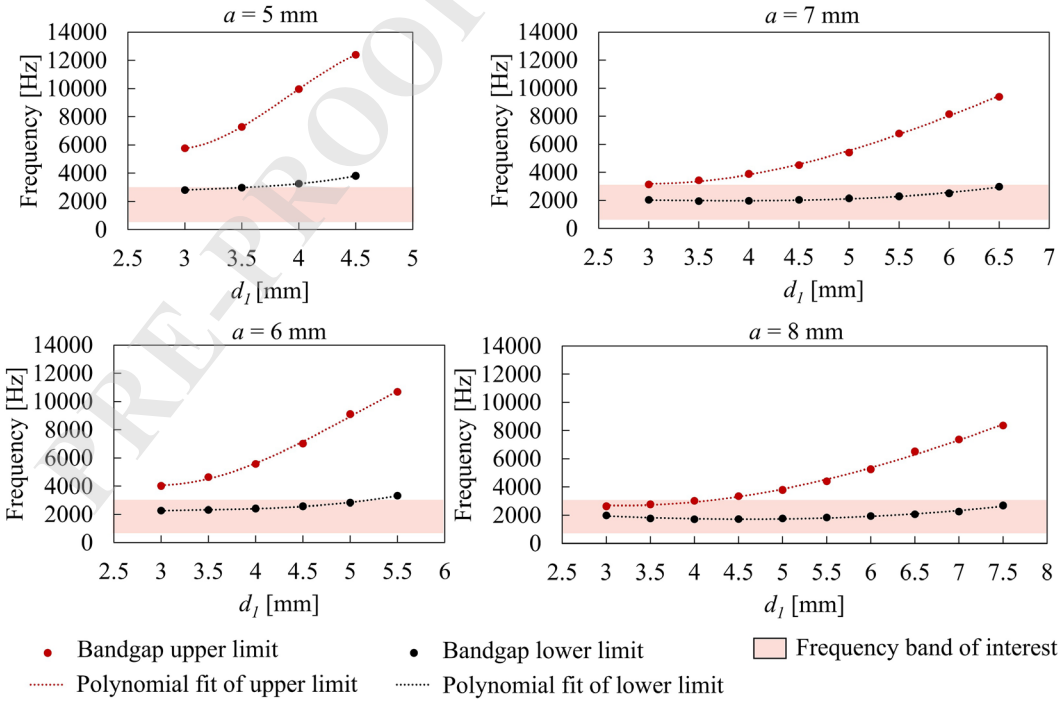

Fig. 7. Bandgap characteristics of metamaterial model 1 for different diameters of inclusion in unit cell with lattice constants depicting the overlapping with frequency range of interest

Results from parametric analysis highlight that the bandgap characteristics are significantly influenced by the inclusion diameter and lattice constant of the metamaterial. As observed in Fig. 7, the upper limit of the bandgap showed significant increase with the increase in the diameter of hard inclusion resulting in the widening of the bandgap. The lower limit of the bandgap also presented gradual increase corresponding to the increase in diameter of hard inclusion. The model 1 with configuration a= 5 mm; d_I=4.5 mm, presented widest bandgap starting from 3820.7 Hz to 12389.6 Hz. The increment of the diameter in case of other configurations having lattice constant a = 6,7 and 8 mm also depicted the similar trend in upper and lower limits of the bandgap frequencies. Importantly, the increase in the lattice constant a showed shifting of the bandgap in downward direction in the dispersion diagrams. The minimum lower limit of the bandgap was observed to be 1708.6 Hz with corresponding upper limit of 3017.7 Hz for the configuration a = 8 mm, d_I = 4 mm in model 1.

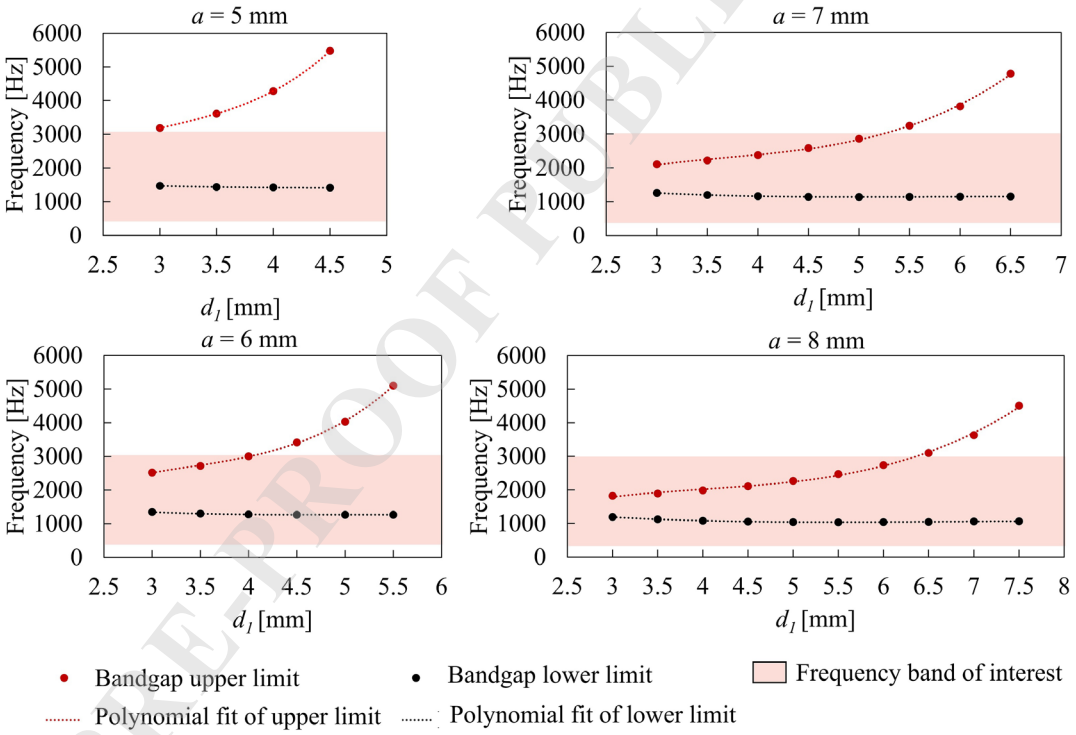

Fig. 8. Bandgap characteristics of metamaterial model 2 with 0.2 mm thick rubber layer for varying diameters of inclusion in unit cell lattice constants depicting the overlapping of the bandgap with the frequency range of interest

The model 2 of elastic metamaterial was analysed to investigate the influence of geometric parameters on the bandgap characteristics. Like case of model 1, the lattice constant was similarly varied from 5 mm to 8 mm with step of 1 mm, and the diameter of the hard inclusion

was changed from 3 mm with step of 0.5 mm, keeping the thickness of soft wrapping layer as 0.2 mm. The results from the parametric analysis of model 2 are presented in Fig. 8. The increase in the inclusion diameter d_1, show significant increase in the upper limit of bandgap but a small decrement in the lower limit of bandgap, leading to the widening of the overall bandgap width. The widest bandgap was observed for the configuration of a = 5 mm; d_1 = 4.5 mm; w = 0.2 mm in the range of 1413.9 Hz to 5466.7 Hz, while the bandgap with minimum lower limit 1034.9 Hz and corresponding upper limit 2472.4 Hz was obtained for a = 8 mm; d_1 = 5.5 mm; w = 0.2 mm, of model 2.

The comprehensive analysis of the parametric study of model 1 and model 2 of metamaterial was conducted to investigate the performance concerning the attenuation of MRI system vibrations as shown in the Fig. 9. The performance factor calculated as % BGC according to equation 8. It was revealed that, the metamaterial model 1 shows maximum 47.83 % BGC for configuration of a = 8 mm, d_1 = 4 mm. In model 2 the maximum of 72.35 % BGC was achieved with configuration of a = 8 mm, d_1 = 6.5 mm and w = 0.2 mm and hence was selected as optimum model for next investigations. Comparing corresponding plots from Fig. 7, 9 and 10, the presence of rubber layer is essential to shift bandgap in lower frequency range.

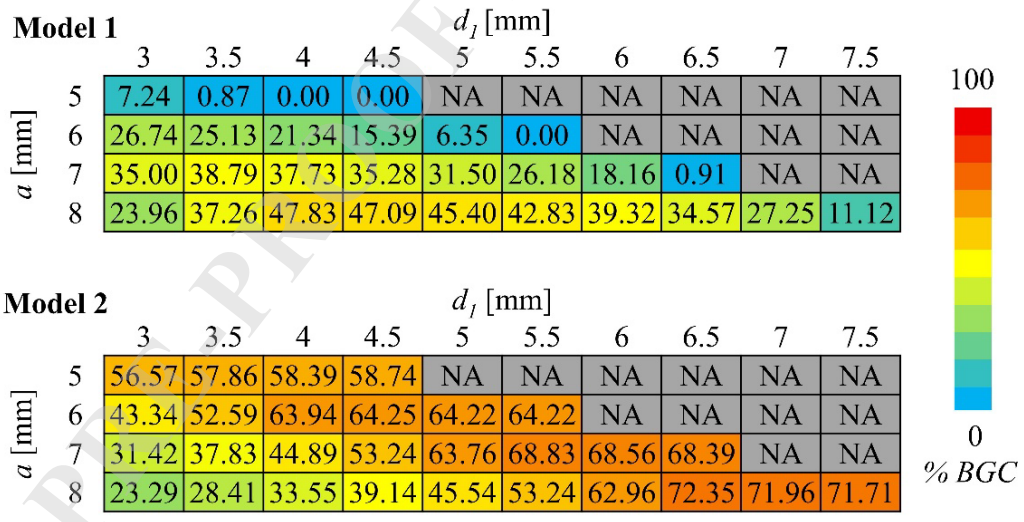

Fig 9. Bandgap coverage percentage (% BGC) calculated for different configuration of metamaterial model 1 and model 2 with wrapping rubber thickness of w = 0.2 mm for the frequency range of interest 300 to 3000 Hz

As the configuration of metamaterial model 2 with inclusion diameter d_1 = 6.5 mm and lattice constant a = 8 mm led to maximum BGC %, it was selected for further evaluation to

investigate the influence of variation of rubber wrapping layer thickness on the bandgap characteristics. The results from the analysis are depicted in Fig. 10. The thickness of the wrapping layer was varied from 0.1 mm to the 0.7 mm with the incremental step size of 0.1 mm. As, the layer thickness was increased, the bandgap shifted in lower frequencies but compromising the width of bandgap. The maximum 72.3% BGC was observed for the configuration with 0.2 mm wrapping layer thickness. Further, increase in thickness resulted in the gradual reduction of BGC from maximum 72.3% to the lowest 50.9%. The lowest frequency associated with opening of bandgap was found to be 650.6 Hz for model 2 with configuration a = 8 mm, d_1 = 6.5 and w = 0.7 mm.

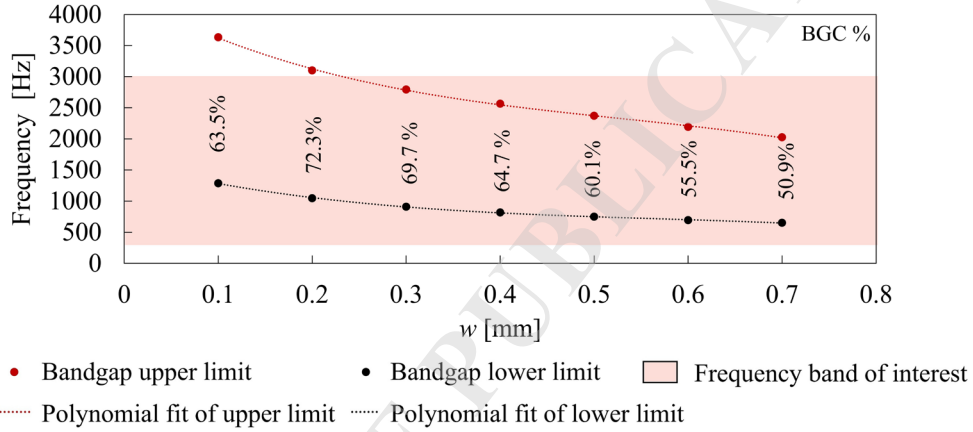

Fig. 10. Bandgap characteristics obtained by variation of wrapping layer thickness w in model 2 with resonator diameter d_1 = 6.5 mm and lattice constant a = 8 mm

The polynomial fit equations of the upper and lower limits of the bandgap from the complete parametric analysis of the model 1 and model 2 are attached in the Appendix 1.

3.3. Frequency domain analysis of optimum model

The unit cell of model 2 presenting maximum 72.3 % BGC identified in previous section was considered for analysing the influence of number of unit cells in elastic wave propagation phenomenon. The transmission loss curves were plotted for arrangement of 3 cells, 4 cells and 5 cells, as shown in Fig. 11. The harmonic input displacement of 0.5 mm was applied to left edge of first cell and response displacement on opposite side of last cell was analysed. The transmission loss in the model was calculated. Results showed that the position of bandgap characteristics concerning frequency range remained same but the vibration attenuation performance *TL was* increased with increase in the number of cells. Also, the results of

displacement propagation in the 5-unit cell model for the frequencies inside and outside the bandgap are shown in Fig. 11. It can be clearly seen that in the bandgap region the wave could not propagate to other side of metamaterial.

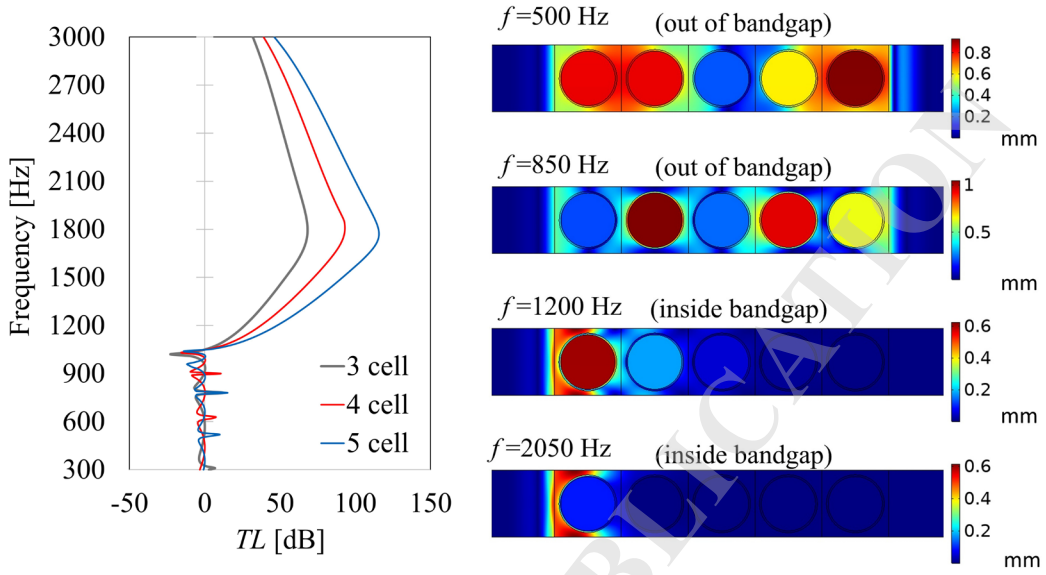

Fig. 11. Transmission loss characteristics calculated for composed system of elastic metamaterial model 2 for 3, 4 and 5 of unit cells with configuration (a = 8 mm, d_1 = 6.5 mm and w =0.2 mm) and displacement wave propagation in metamaterial model 2, with 5-unit cells for different input frequencies

Study demonstrated that a high contrast in the physical properties of the constituent materials can produce local resonance bandgaps in mid-range frequencies such as 300 to 3000 Hz, advancing the conventional metamaterials with size of unit cells in few centimetres for targeting similar frequency range (Gao et al., 2023; Yin et al., 2024). The material selection was challenging due MRI specific and medical requirements. Model 2 with an optimum configuration reported BGC of 72.3 % and high transmission loss within bandgaps, suggesting potential for reducing the vibro-acoustic coupling at air-structure interface. Although optimum model covers high noise frequency zone, the frequencies below the bandgap may still contribute to noise. Hence, it is important to explore more possibilities to fully cover the MRI noise spectra. Currently, the weight of the identified metamaterial is higher considering the larger fill fraction of the high-density inclusion, the future work will focus on enhancing the attenuation capabilities of elastic metamaterial while ensuring it to be lightweight and non-magnetic for compatibility with MRI environment.

4. Conclusion

In summary, two models of elastic metamaterial compose of soft silicone matrix, rubber layer and hard tungsten cylindrical inclusions were analysed for targeted vibration attenuation of MRI gradient coil frequencies. It was found that the both the models show bandgaps in desired frequency range but the BCG of model 1 was very low as compared to model 2. As observed in model 1, the bandgap shifted in lower frequencies with increase in the inclusion diameter but could not achieve BGC more than 47.83 % with opening of bandgap at 1708.6 Hz. While the optimum configuration of model 2 showed up to 72.3% BGC with the lower opening of bandgap at 1046.6 Hz.

The characteristics of the presented elastic metamaterial are highly dependent on the geometric parameters. The parametric analysis revealed that higher values of inclusion diameter, lattice constant and thickness of the soft layer shift the bandgap towards lower frequencies, but narrow the bandgap width. Frequency-domain analysis demonstrated significant transmission loss within the bandgap, validating the vibration attenuation performance. Results suggest that further studies should focus on increasing bandgap coverage through exploring multi-material configuration for enhanced performance.

Overall, numerical study highlights the capability of the elastic metamaterials in attenuating the MRI-induced vibration, and the high transmission loss in bandgap suggests that the presented elastic metamaterial may provide a means to reduce vibro-acoustic coupling in MRI systems.

Appendix A.

Trendline curves of the bandgap limits in Model 1 from parametric analysis:

Configuration	Upper limit of the bandgap	Lower limit of the bandgap
$a = 5\,mm$, $d_1 \in [3, 4.5]$	$f_{g2} = -1864.1{d_1}^3 + 21880{d_1}^2 - 79995d_1 + 99160$	$f_{g1} = 222.27{d_1}^3 - 2111.4{d_1}^2 + 7011.1d_1 - 5227.6$
$a = 6\,mm$, $d_1 \in [3, 5.5]$	$f_{g2} = -277.3{d_1}^3 + 4202.4{d_1}^2 - 17597d_1 + 26525$	$f_{g1} = 80.29{d_1}^3 - 818.66{d_1}^2 + 2903.8d_1 - 1239.3$
$a = 7\,mm$, $d_1 \in [3, 6.5]$	$f_{g2} = -53.57{d_1}^3 + 1181.9d_1 2 - 5653.8d_1 + 10967$	$f_{g1} = 23.636{d_1}^3 - 197.09{d_1}^2 + 462.25d_1 + 1780.1$
$a = 8\,mm$, $d_1 \in [3, 7.5]$	$f_{g2} = -20.172{d_1}^3 + 591.54{d_1}^2 - 3166.2d_1 + 7421.9$	$f_{g1} = 4.7403{d_1}^3 + 30.757{d_1}^2 - 582.69d_1 + 3286.3$

Trendline curves of the bandgap limits of Model 2 from parametric analysis:

Configuration	Upper limit of the bandgap	Lower limit of the bandgap
$a = 5\,mm$, $w = 0.2\,mm$, $d_1 \in [3, 4.5]$	$f_{g2} = 361.56{d_1}^3 - 3308.8{d_1}^2 + 10883d_1 - 9448.6$	$f_{g1} = -20.277{d_1}^3 + 253.14{d_1}^2 - 1070.6d_1 + 2953.3$
$a = 6\,mm$, $w = 0.2\,mm$, $d_1 \in [3, 5.5]$	$f_{g2} = 156.2{d_1}^3 - 1586.6{d_1}^2 + 5809.9d_1 - 4857.8$	$f_{g1} = -10.95{d_1}^3 + 164.3{d_1}^2 - 818.35d_1 + 2618.9$
$a = 7\,mm$, $w = 0.2\,mm$, $d_1 \in [3, 6.5]$	$f_{g2} = 77.66{d_1}^3 - 864.36{d_1}^2 + 3479.1d_1 - 2667.8$	$f_{g1} = -6.4297{d_1}^3 + 113.04{d_1}^2 - 648.65d_1 + 2359.7$
$a = 8\,mm$, $w = 0.2\,mm$, $d_1 \in [3, 7.5]$	$f_{g2} = 43{d_1}^3 - 519.71{d_1}^2 + 2277.3d_1 - 1526.4$	$f_{g1} = -4.1224{d_1}^3 + 82.899{d_1}^2 - 536.63d_1 + 2164.7$
$a = 8\,mm$, $d_1 = 6.5\,mm$, $w \in [0.1, 0.7]$	$f_{g2} = -7708.7w^3 + 12277w^2 - 8101.6w + 4317$	$f_{g1} = -3417.4w^3 + 5814.9w^2 - 3762.6w + 1604.1$

FUNDINGS

This work was supported and financed by Department of Mechanics and Vibroacoustics, Faculty of Mechanical Engineering and Robotics, AGH University of Krakow, in Kraków, Poland, from the finance source: 10000.501.00.130000.

CONFLICT OF INTEREST

The authors declare that they have no known competing financial interests or personal relationships that could have appeared to influence the work reported in this paper.

AUTHORS' CONTRIBUTION

Swapnil Arawade conceptualized the study and wrote the original draft of manuscript, conducted formal analysis, interpretation of the results; Janusz Piechowicz performed the supervision, contributed to data interpretation, review and editing of manuscript and fund acquisition. All authors reviewed and approved the final manuscript.

DATA AVAILABILITY STATEMENT

The data that support the findings of this study are available from the corresponding author upon reasonable request.

References

1. Bruno F., Arrigoni F., Mariani S., Splendiani A., Di Cesare E., Masciocchi C. and Barile A. (2019), Advanced magnetic resonance imaging (MRI) of soft tissue tumors: techniques and

applications, *La radiologia medica*, 124, pp.243-252. https://doi.org/10.1007/s11547-019-01035-7

2. Reda R., Zanza A., Mazzoni A., Cicconetti A., Testarelli L. and Di Nardo D. (2021), An update of the possible applications of magnetic resonance imaging (MRI) in dentistry: a literature review, *Journal of imaging*, 7(5), p.75. https://doi.org/10.3390/jimaging7050075

3. Landini L., Mainardi L.T., Positano V., Young A.A., Santarelli M., Ying L., Kyriakos W.E., den Dekker A.J., Styner M., Halchenko Y.O. and Frangi A. (2018), Advanced image processing in magnetic resonance imaging, CRC press. https://doi.org/10.1201/9781420028669

4. Zhang Y., Kong X., He W. and Xu Z. (2025), Eddy Current Characterization Using Efficient Finite Element Analysis for Z-Gradient Coils in a Low-field MRI Scanner, *IEEE Transactions on Instrumentation and Measurement*, 74, 1-9. https://doi.org/10.1109/TIM.2025.3544743

5. Leo P. and D'Orazio A. (2025), Lorentz force and vibrations in transverse gradient coils in MRI, *International Journal of Mechanical Sciences*, p.110011. https://doi.org/10.1016/j.ijmecsci.2025.110011

6. Hedeen R.A. and Edelstein W.A. (1997), Characterization and prediction of gradient acoustic noise in MR imagers, *Magnetic Resonance in Medicine*, 37(1), pp.7-10. https://doi.org/10.1002/mrm.1910370103

7. Mansfield P., Glover P.M. and Beaumont J. (1998), Sound generation in gradient coil structures for MRI, *Magnetic resonance in medicine*, 39(4), pp.539-550. https://doi.org/10.1002/mrm.1910390406

8. Moelker A., Wielopolski P.A. and Pattynama P.M. (2003), Relationship between magnetic field strength and magnetic-resonance-related acoustic noise levels, *Magnetic Resonance Materials in Physics*, Biology and Medicine, 16, pp.52-55. https://doi.org/10.1007/s10334-003-0005-9

9. Moelker A. and Pattynama P.M. (2003), Acoustic noise concerns in functional magnetic resonance imaging, *Human brain mapping*, 20(3), pp.123-141. https://doi.org/10.1002/hbm.10134

10. Hutter J., Price A.N., Cordero-Grande L., Malik S., Ferrazzi G., Gaspar A., Hughes E.J.,

Christiaens D., McCabe L., Schneider T. and Rutherford M.A. (2018), Quiet echo planar imaging for functional and diffusion MRI, *Magnetic resonance in medicine*, 79(3), pp.1447-1459. https://doi.org/10.1002/mrm.26810

11. Arawade S. and Piechowicz J. (2024), Spectral Analysis of MRI Sound Signal, *International Journal of Electronics and Telecommunications*, pp.839-847. DOI: 10.24425/ijet.2024.152068

12. Arawade S. and Piechowicz J. (2024), Acoustic characterization of the 1.5 Tesla MRI facility in Mobile Imaging Trailer, *Vibrations in Physical Systems*, 34(2),20242019. http://dx.doi.org/10.21008/j.0860-6897.2024.2.19

13. Gallichan D., Scholz J., Bartsch A., Behrens T.E., Robson M.D. and Miller K.L. (2010), Addressing a systematic vibration artifact in diffusion-weighted MRI, *Human brain mapping*, 31(2), pp.193-202. https://doi.org/10.1002/hbm.20856

14. Fuhrer E., Jouda M., Klein C.O., Wilhelm M. and Korvink J.G. (2019), Gradient-induced mechanical vibration of neural interfaces during MRI, *IEEE Transactions on Biomedical Engineering*, 67(3), pp.915-923 https://doi.org/10.1109/TBME.2019.2923693

15. Frollo I., Andris P., Pribil J. and Juras V. (2007), Indirect susceptibility mapping of thin-layer samples using nuclear magnetic resonance imaging, *IEEE transactions on magnetics*, 43(8), pp.3363-3367. https://doi.org/10.1109/TBME.2019.2923693

16. McJury M.J. (2022), Acoustic noise and magnetic resonance imaging: a narrative/descriptive review, *Journal of Magnetic Resonance Imaging*, 55(2), pp.337-346. https://doi.org/10.1002/jmri.27525

17. Kanal E., Shellock F.G. and SMRI Safety Committee (1992), Policies, guidelines, and recommendations for MR imaging safety and patient management, *journal of magnetic resonance imaging*, 2(2), pp.247-248. https://doi.org/10.1002/jmri.1880020222

18. AlMeer M.H. (2022), MRI Acoustic Noise cancellation using CNN, *Journal of Engineering Research*, https://doi.org/10.36909/jer.17661

19. Li M., Rudd B., Lim T.C. and Lee J.H. (2011), In situ active control of noise in a 4 T MRI scanner, *Journal of Magnetic Resonance Imaging*, 34(3), pp.662-669. https://doi.org/10.1002/jmri.22694

20. Lee N., Park Y. and Lee G.W. (2017), Frequency-domain active noise control for magnetic resonance imaging acoustic noise, *Applied Acoustics*, 118, pp.30-38. https://doi.org/10.1016/j.apacoust.2016.11.003

21. Lasota A. and Meller M. (2020), Iterative learning approach to active noise control of highly autocorrelated signals with applications to machinery noise, *IET Signal Processing*, 14(8), pp.560-568. https://doi.org/10.1049/iet-spr.2020.0064

22. AMC MECANOCAUCHO, Vibrabsorber + Sylomer® Vibration Isolation Systems, https://www.mecanocaucho.com/en/news/magnetic-resonance-en/, (access: 26/10/2025).

23. Kinetics Noise Control, Precision Isolation Systems for Sensitive Equipment, https://kineticsnoise.com/precision/isolation , (access: 26/10/2025).

24. Unisorb Installation Technologies, Vibration Isolation Systems for Medical Equipment, https://unisorb.com/industries/medical-equipment/, (access: 26/10/2025).

25. International Design Engineering (IDE), Active Vibration Isolation, https://www.ideworld.com/en/active_vibration_isolation.html, (access: 26/10/2025).

26. Acoustical Surfaces Inc, Soundproofing a Noisy MRI Scanner, blog post, 22 September 2008, https://www.acousticalsurfaces.com/blog/soundproofing/soundproofing-a-noisy-mri-scanner/ ,(access: 26/10/2025).

27. Faraday Shielding and Design Pvt Ltd, Acoustic Wall Panels, https://faradayshielding.com.au/acoustic-wall-panels-2/, (access: 26/10/2025)

28. Kumar R., Kumar M., Chohan J.S. and Kumar S. (2022), Overview on metamaterial: History, types and applications, *Materials Today: Proceedings*, 56, pp.3016-3024. https://doi.org/10.1016/j.matpr.2021.11.423

29. Wei Y., Pan F., Lin X., Zhang L., Xiang J. and Chen Y. (2025), On-demand Reprogrammable Mechanical Metamaterial Driven by Structure Performance Relations, *Advanced Materials*, 37(9), p.2410865. https://doi.org/10.1002/adma.202410865

30. Wu X., Yan H., Zhou Y., Zhang P., Lu Q. and Shi H. (2025), Review of additive manufactured metallic metamaterials: Design, fabrication, property and application, *Optics & Laser Technology*, 182, p.112066. https://doi.org/10.1016/j.optlastec.2024.112066

31. Zhang W. and Zhao Y. (2025), Sound absorption characteristics of the metamaterial with stochastic parameters, *International Journal of Mechanical Sciences*, 287, p.109929. https://doi.org/10.1016/j.ijmecsci.2025.109929

32. Miao Z., Yin J., Yang Y., Ke Y., Zheng Z., Geng X. and Wang Q. (2025), Design of multi-bandgap metamaterial plate based on composite cylindrical resonators, *Materials & Design*, 250, p.113570. https://doi.org/10.1016/j.matdes.2024.113570

33. Liu X., Chen S., Wang B., Tan X., Cao B. and Yu L. (2025), A mechanical metamaterial with real-time tunable bandgap based on pneumatic actuation, *International Journal of Mechanical Sciences*, p.110045. https://doi.org/10.1016/j.ijmecsci.2025.110045

34. Ahmad M.J., Tian X., Dai X., Wu L., Zia A.A., Ghafoor S. and Li W. (2025), Non-conformal thermal cloak metamaterial by continuous metal fiber embedded 3D printing, *International Journal of Heat and Mass Transfer*, 242, p.126796. https://doi.org/10.1016/j.ijheatmasstransfer.2025.126796

35. Fu Y., Huang X., Luo Y., Guo L., Liang J., Jin J. and Yang H. (2025), A Multi-Polarization Multi-Band Reconfigurable Cloaking-Illusion Metasurface, *Advanced Optical Materials*, 13(4), p.2402381. https://doi.org/10.1002/adom.202402381

36. Ruks L., Ballantine K.E. and Ruostekoski J. (2025), Negative refraction of light in an atomic medium, *Nature Communications*, 16(1), p.1433. https://doi.org/10.1038/s41467-025-56250-w

37. Zhou Y., Sang T. and Wang Y. (2025), Negative Refraction Guided by a Glide-Reflection Symmetric Crystal Interface, *Materials*, 18(6), p.1210. https://doi.org/10.3390/ma18061210

38. Hao L., Guo J., Liu, D., Yan X., Yang Q., Tian X., Huang K., Pang S., Xie Y. and Chen Z. (2025), Tunable Tri-band Negative Mass Density Acoustic Metamaterials with Nested Three-layer Hollow Tubes, *Physica B: Condensed Matter*, p.417194. https://doi.org/10.1016/j.physb.2025.417194

39. Wang Z., Shen Y., Tan J., Yang H., Peng P., Liu F. and Du Q. (2025), A broadband zero-frequency seismic metamaterial based on negative effective mass density, *Physics Letters A*, 531, p.130151. https://doi.org/10.1016/j.physleta.2024.130151

40. Li Y. (2025), A Review on Porous Structure Negative Poisson's Ratio Metamaterials,

Journal of Engineering Research and Reports, 27(1), pp.189-204. https://doi.org/10.9734/jerr/2025/v27i11378

41. Shunshun R. and Zhao G. (2025), Mechanical characterization of a metamaterial with negative Poisson's ratio under compressive loading: Experimental along with FEM, *Mechanics of Advanced Materials and Structures*, pp.1-10. https://doi.org/10.1080/15376494.2025.2477229

42. Chua J.W., Poh D.K.W., Ding S., Pei H. and Li X. (2025), Unveiling the structure-property relationships of multilayered Helmholtz resonance-based acoustic metamaterials, *Smart Materials in Manufacturing*, 3, p.100073. https://doi.org/10.1016/j.smmf.2025.100073

43. He Y., Bi Z., Wang T., Wang L., Lu G., Cui Y. and Tse K.M. (2024), Design and mechanical properties analysis of hexagonal perforated honeycomb metamaterial, *International Journal of Mechanical Sciences*, 270, p.109091. https://doi.org/10.1016/j.ijmecsci.2024.109091

44. Kaina N., Fink M., & Lerosey, G. (2013), Composite media mixing Bragg and local resonances for highly attenuating and broad bandgaps, *Scientific Reports*, 3. https://doi.org/10.1038/srep03240

45. Chuang K. C., Yuan Z. W., Guo Y. Q., & Lv X. F. (2020), Extracting torsional band gaps and transient waves in phononic crystal beams: Method and validation, *Journal of Sound and Vibration*, 467. https://doi.org/10.1016/j.jsv.2019.115004

46. Liu M., & Zhu W. D. (2019), Modeling and analysis of in-plane and out-of-plane elastic wave propagation in a phononic-crystal circular beam, *Journal of Sound and Vibration*, 462. https://doi.org/10.1016/j.jsv.2019.114886

47. Qi X.Q., Li T.J., Zhang J.L., Zhang Z. and Tang Y.Q., (2018), Band gap structures for 2D phononic crystals with composite scatterer, *Applied Physics A*, 124(5), p.364. https://doi.org/10.1007/s00339-018-1789-9

48. Xiang H., Ma X., & Xiang J. (2020), Band gaps and transmission characteristics analysis on a two-dimensional multiple-scatter phononic crystal structure, *Materials*, 13(9). https://doi.org/10.3390/ma13092106

49. Wen S., Xiong Y., Hao S., Li F., & Zhang C. (2020), Enhanced band-gap properties of an

acoustic metamaterial beam with periodically variable cross-sections, *International Journal of Mechanical Sciences,* 166. https://doi.org/10.1016/j.ijmecsci.2019.105229

50. Wickeler A. L., & Naguib H. E. (2020), Novel origami-inspired metamaterials: Design, mechanical testing and finite element modelling, *Materials and Design*, 186. https://doi.org/10.1016/j.matdes.2019.108242

51. Zhao H., Zhang E., & Lu G. (2024), Study on the Equivalent Stiffness of a Local Resonance Metamaterial Concrete Unit Cell, *Buildings*, 14(4). https://doi.org/10.3390/buildings14041035

52. Lee S. H., & Wright O. B. (2016), Origin of negative density and modulus in acoustic metamaterials, *Physical Review B*, 93(2). https://doi.org/10.1103/PhysRevB.93.024302

53. Lee G., Lee D., Park J., Jang Y., Kim M. and Rho J., (2022), Piezoelectric energy harvesting using mechanical metamaterials and phononic crystals, *Communications Physics*, 5(1), pp.94. https://doi.org/10.1038/s42005-022-00869-4

54. Hu G., Tang L., Xu J., Lan C., & Das R. (2019), Metamaterial with Local Resonators Coupled by Negative Stiffness Springs for Enhanced Vibration Suppression, *Journal of Applied Mechanics*, Transactions ASME, 86(8). https://doi.org/10.1115/1.4043827

55. Li G., Chen Y., Chen W., Liu J., & He H. (2022), Local resonance – Helmholtz lattices with simultaneous solid-borne elastic waves and air-borne sound waves attenuation performance, *Applied Acoustics*, 186. https://doi.org/10.1016/j.apacoust.2021.108450

56. Peiró-Torres M. P., Castiñeira-Ibáñez S., Redondo J., & Sánchez-Pérez J. V. (2019), Interferences in locally resonant sonic metamaterials formed from Helmholtz resonators, *Applied Physics Letters*, 114(17). https://doi.org/10.1063/1.5092375

57. Naify C. J., Chang C. M., McKnight G., & Nutt S. (2010), Transmission loss and dynamic response of membrane-type locally resonant acoustic metamaterials, *Journal of Applied Physics*, 108(11). https://doi.org/10.1063/1.3514082

58. Fan L., He Y., Chen X. A., & Zhao X. (2021), A frequency response function-based optimization for metamaterial beams considering both location and mass distributions of local resonators, *Journal of Applied Physics*, 130(11). https://doi.org/10.1063/5.0059025

59. Hu G., C. M. Austin A., Sorokin V., & Tang L. (2021), Metamaterial beam with graded local

resonators for broadband vibration suppression, *Mechanical Systems and Signal Processing*, 146. https://doi.org/10.1016/j.ymssp.2020.106982

60. Ma G. and Sheng P., (2016), Acoustic metamaterials: From local resonances to broad horizons, *Science advances*, 2(2), p.e1501595. https://doi.org/10.1126/sciadv.1501595

61. Pires F. A., Sangiuliano L., Denayer H., Deckers E., Desmet W., & Claeys C. (2022), The use of locally resonant metamaterials to reduce flow-induced noise and vibration, *Journal of Sound and Vibration*, 535. https://doi.org/10.1016/j.jsv.2022.117106

62. Sun P., Guo H., Jin F., Zhang Z., Liu N., Yuan T., Ma L. and Wang Y. (2022), Mechanics and extreme low-frequency band gaps of auxetic hexachiral acoustic metamaterial with internal resonant unit, *Applied Acoustics*, 200, p.109046. https://doi.org/10.1016/j.apacoust.2022.109046

63. Huang T.T., Ren X., Zeng Y., Zhang Y., Luo C., Zhang X.Y. and Xie Y.M. (2021), Based on auxetic foam: A novel type of seismic metamaterial for Lamb waves, *Engineering Structures*, 246, p.112976. https://doi.org/10.1016/j.engstruct.2021.112976

64. Li Y., Yan S. and Peng Y. (2023). Broadband vibration attenuation characteristic of 2D phononic crystals with cross-like pores, *Thin-Walled Structures*, 183, p.110418. https://doi.org/10.1016/j.tws.2022.110418

65. Yang H.Y., Cheng S.L., Li X.F., Yan Q., Wang B., Xin Y.J., Sun Y.T., Ding, Q. Yan, H. and Zhao Q.X. (2023), Low frequency elastic waves and vibration control mechanism of innovative phononic crystal thin plates, *Physica B: Condensed Matter*, 667, p.415189. https://doi.org/10.1016/j.physb.2023.415189

66. Tang R., Lu T. and Zheng W. (2024), Low-frequency ultrawide band gap study of symmetric conical scatterer phononic crystal, *Journal of Vibration Engineering & Technologies*, 12(3), pp.3667-3676. https://doi.org/10.1007/s42417-023-01077-2

62. Enghag P. (2008), *Encyclopedia of the elements: technical data-history-processing-applications*, John Wiley & Sons.

63. Wapler, M.C., Leupold, J., Dragonu, I., von Elverfeld, D., Zaitsev, M. and Wallrabe, U. (2014), Magnetic properties of materials for MR engineering, micro-MR and beyond, *Journal*

of magnetic resonance, 242, pp.233-242. https://doi.org/10.1016/j.jmr.2014.02.005

64. Callister Jr, W.D. and Rethwisch, D.G. (2020). *Callister's materials science and engineering*, John Wiley & Sons.

65. Schenck J.F. (1996), The role of magnetic susceptibility in magnetic resonance imaging: MRI magnetic compatibility of the first and second kinds, *Medical physics*, 23(6), pp.815-850. https://doi.org/10.1118/1.597854

66. Kajima Y., Takaichi A., Tsutsumi Y., Hanawa T., Wakabayashi N., & Kawasaki A. (2020), Influence of magnetic susceptibility and volume on MRI artifacts produced by low magnetic susceptibility Zr-14Nb alloy and dental alloys, *Dental materials journal*, 39(2), 256–261. https://doi.org/10.4012/dmj.2018-426

67. Chiba Y., Murakami H., Sasaki M., Endo H., Yamabe D., Kinno D., & Doita M. (2019), Quantification of metal-induced susceptibility artifacts associated with ultrahigh-field magnetic resonance imaging of spinal implants, *JOR spine,* 2(3), e1064. https://doi.org/10.1002/jsp2.1064

68. Buchli R., Boesiger, P. & Meier D. (1988), Heating effects of metallic implants by MRI examinations, *Magnetic resonance in medicine*, 7(3), 255-261. https://doi.org/10.1002/mrm.1910070302

69. Stroud J., Stupic K., Walsh T., Celinski Z., & Hankiewicz J. H. (2019, March), Local heating of metallic objects from switching magnetic gradients in MRI. In *Medical Imaging 2019: Imaging Informatics for Healthcare, Research, and Application,* Vol. 10954, pp. 150-161, SPIE, San Diego, California, United States. https://doi.org/10.1117/12.2512903

70. Lee S. K., Tarasek M., Li K., & Spence D. K. (2024), Eddy current heating of metallic shells and plates: application to gradient-induced conductor heating in MRI, *IEEE Transactions on Magnetics*. https://doi.org/10.1109/TMAG.2024.3432915

71. Mattei E. et al. (2008), Complexity of MRI induced heating on metallic leads: experimental measurements of 374 configurations, *Biomedical engineering online*, 7(1), 11. https://doi.org/10.1186/1475-925X-7-11

72. Winter L., Seifert F., Zilberti L., Murbach M., & Ittermann B. (2021), MRI-related heating of implants and devices: a review, *Journal of Magnetic Resonance Imaging*, 53(6), 1646-1665.

https://doi.org/10.1002/jmri.27194

73. Gao W., Zhang Q., Sun J. and Guo K., (2023), A novel 3D-printed magnesium alloy phononic crystal with broadband bandgap. *Journal of Applied Physics*, 133(8). https://doi.org/10.1063/5.0135770

74. Yin W., Zhu J., Tong Z., Wang L., Li D. and Wang L., (2024), 3D printed three-dimensional elastic metamaterial with surface resonant units for low-frequency vibration isolation. *Virtual and Physical Prototyping*, 19(1), p.e2382159. https://doi.org/10.1080/17452759.2024.2382159